Stretchable OFET memories: Tuning the morphology and charge-trapping ability of conjugated block copolymers through soft segment branching

Li-Che Hsu[1,2], Takuya Isono[3], Yan-Cheng Lin[4], Saburo Kobayashi[2], Yun-Chi Chiang[4], Dai-Hua Jiang[1,2], Chih-Chien Hung[5], Ender Ercan[5], Wei-Chen Yang[4], Hui-Ching Hsieh[4], Kenji Tajima[3], Toshifumi Satoh[3], and Wen-Chang Chen[1,4,5]**

[1]Institute of Polymer Science and Engineering, National Taiwan University, Taipei 10617, Taiwan

[2]Graduate School of Chemical Sciences and Engineering, Hokkaido University, Sapporo 060-8628, Japan

[3]Faculty of Engineering, Hokkaido University, Sapporo 060-8628, Japan

[4]Department of Chemical Engineering, National Taiwan University, Taipei 10617, Taiwan

[5]Advanced Research Center for Green Materials Science and Technology, National Taiwan University, Taipei 10617, Taiwan

Keywords: organic field-effect transistors, charge-trapping, polyfluorene, poly(δ-decanolactone), block copolymers, stretchable memory device

ABSTRACT

The mechanical properties and structural design flexibility of charge-trapping polymer electrets has led to their widespread use in organic field-effect transistor (OFET) memories. For example, in the electrets of polyfluorene-based conjugated/insulating block copolymers (BCPs), the confined fiber-like polyfluorene nanostructures in the insulating polymer matrix act as effective hole-trapping sites, leading to controllable memory performance through the design of BCP. However, few studies have reported intrinsically stretchable charge-trapping materials and their memory device applications, and a practical method to correlate thin film morphology of BCP electrets with their charge-trapping ability has not yet been developed. In this study, a series of new conjugated/insulating BCPs, poly(9,9-di-n-hexyl-2,7-fluorene)-*block*-poly(*δ*-decanolactone)s (PF-*b*-PDL$_x$, x = 1-3) as stretchable hole-trapping materials are reported. The linear and branched PDL blocks with the comparable molecular weight were used to investigate the effect of polymer architecture on morphology and device performance. Moreover, coverage area of the polyfluorene nanofibers on the BCP films was extracted from atomic force microscopy images, which can be correlated with the trapping density of the polymer electrets. The branched PDL segments not only improve stretchability but also tailor crystallinity and phase separation of the BCPs, thus increasing their charge-trapping ability. The OFET memory device with PF-*b*-PDL$_3$ as electret layer exhibited the largest memory window (102 V), and could retain its performance at up to 100% strain. This research highlights the importance of BCP design for developing stretchable charge-trapping materials.

INTRODUCTION

In recent years, organic and polymer-based electronic devices have drawn extensive research attention in response to the booming demand for wearable electronic products,[1-3] Sensors,[4-6] transistors,[7-9] and memories[10-12] based on organic materials, and their integrated wearable devices,[13-16] have been vigorously developed. Among various types of organic memory devices, organic field-effect transistor (OFET) memories are particularly attractive owing to their non-destructive read-out and manufacturing compatibility with integrated circuits composed of OFETs. OFET memories are also low-cost, light-weight, and offer mechanical flexibility and solvent processibility, which are expected to provide excellent alternatives to traditional Si-based memories.[17-18] An OFET memory cell is a conventional transistor with a charge-storage layer sandwiched between an organic semiconducting layer and a dielectric layer. The charge-storage layer is the key component in OFET memory since it can trap positive or negative charges through an additional electric field (gate bias). Therefore, charge distribution in the semiconducting layer can be changed to modulate its high conducting and low conducting states.

Three major types of charge-trapping materials that have been widely used as the charge-storage layer of OFET memories are metallic nano-floating-gate dielectrics,[19-20] organic ferroelectric materials,[21-22] and polymer electrets.[23-24] Polymer-based electrets have drawn tremendous research attention recently, owing to their advanced mechanical properties and flexibility in terms of chemical structural design.[25] Among various kinds of polymer electrets, polyfluorene-based materials are particularly promising due to desirable energy levels and charge-trapping ability. Several processing or synthetic strategies, such as conjugated/insulating polymer blends,[26-27] self-doped nanostructures of polyfluorene,[28] pendent fluorene moieties with different conjugation length,[29] and polyfluorene-based block copolymers (BCPs),[30] have been proposed to facilitate

charge-trapping within polymer thin films. However, as a result of the rigid polymer backbone of conjugated polymers, the materials in the above examples are still incapable of enduring high mechanical strain for stretchable device applications.

To improve the mechanical properties of conjugated polymers, one useful strategy is to create BCPs with conjugated and soft elastic blocks. For example, polythiophene-based conjugated/elastic BCPs have been developed as stretchable semiconducting materials.[31-32] The incorporated soft segments provide a degree of freedom for the movement of polymer chains, leading to enhanced mechanical properties of the conjugated polymers. In a more relevant study on polyfluorene, a linear diblock copolymer consisting of poly(9,9-di-*n*-hexyl-2,7-fluorene) and poly(*n*-butyl acrylate) (PF-*b*-PBA)[33] was synthesized to investigate the effect of stress on the optical properties of the BCP. However, polyfluorene-based BCPs as polymer electrets for stretchable OFET memory applications have not yet been reported.

In this work, we demonstrate novel stretchable polyfluorene-based miktoarm BCPs as hole-trapping materials. The incorporated soft segments with different structures are expected to not only provide elastic properties but also tailor phase separation and charge trapping sites within the polymer thin films. A series of polyfluorene-based linear and branched BCPs containing poly(9,9-di-*n*-hexyl-2,7-fluorene) (PF) and poly(*δ*-decanolactone) (PDL), denoted as PF-*b*-PDL, PF-*b*-PDL_2, and PF-*b*-PDL_3, were designed as the charge-storage layer of an n-type *N*,*N*′-dioctyl-3,4,9,10-perylenedicarboximide (PTCDI-C8)-based OFET memory. Note that PDL is a bio-based amorphous polymer with a glass transition temperature below -60 °C, which is an environmental-friendly candidate for creating BCPs with soft segments.[34] The crystallization processes of the BCPs were investigated with differential scanning calorimetry (DSC), and the energy levels were determined by UV-vis absorption spectroscopy and cyclic voltammetry (CV). Moreover, we

propose a new protocol to correlate the film morphology of the BCP electret with its charge-trapping properties. The PF nanofibers confined within an insulting polymer matrix are regarded as efficient hole-trapping sites in the polymer electret.[30] In the present study, we quantitatively analyzed the width (W), length (L) and coverage area (A%) of the PF nanofibers within the BCP thin films using atomic force microscopy (AFM) phase images, and those features were correlated with the charge trapping density of the OFET memories. This method is useful for evaluating nanostructures of BCP thin films for advanced device applications. In the last section, we investigated the stretchability of the polymer thin films using optical microscopy (OM). OFET memory devices fabricated with the stretched and transferred charge-storage layer were also examined to assess the performance of the charge-trapping materials under stretching conditions.

EXPERIMENTAL SECTION

Materials. Tetrahydrofuran (THF, anhydrous, ≥99.9%), methanol (MeOH, anhydrous, 99.8%), toluene (≥99.8%), *N*,*N*,*N*',*N*'',*N*''-pentamethyldiethylenetriamine (PMDETA, 99%), copper(I) bromide (CuBr, 98%), trichloroethylene (TCE, anhydrous, ≥99%), ammonium hydroxide solution (ammonia water, 28.0-30.0%), PTCDI-C8 (98%), and polydimethylsiloxane (PDMS, Sylgard 184) were purchased from Sigma-Aldrich Co. (St. Louis, MO); *n*-octadecyltrichlorosilane (ODTS, 97%) was purchased from Gelest Inc. (Morrisville, PA). The above chemicals were used as received without further purification.

Polymer Synthesis. The synthetic route for the target polymers is shown in **Scheme 1**. Alkyne functionalized PF (alkyne-PF) and azido functionalized PDLs (N_3-PDL_x, x = 1-3) were prepared as the building blocks for the target BCPs. Poly(9,9-di-*n*-hexyl-2,7-fluorene) with a benzyl alcohol group at α chain-end ($HOCH_2$-PF) was synthesized through modified Suzuki-Miyaura coupling

polymerization according to our previous report.[35] Esterification reaction between $HOCH_2$-PF and 5-hexynoic acid was then performed to produce alkyne-PF.[36] The azido functionalized poly(*δ*-decanolactone)s with linear, two-armed, and three-armed structures, denoted as N_3-PDL, N_3-PDL_2, and N_3-PDL_3, respectively, were synthesized by living ring-opening polymerization following our previous report.[32] AB, AB_2, and AB_3 type polymers (A = PF, B = PDL) were then synthesized via Cu-catalyzed azido–alkyne click reaction (CuAAC) between alkyne-PF and N_3-PDL_x (x = 1-3) homopolymers. Further details related to the polymer synthesis are provided in the Supporting Information**.**

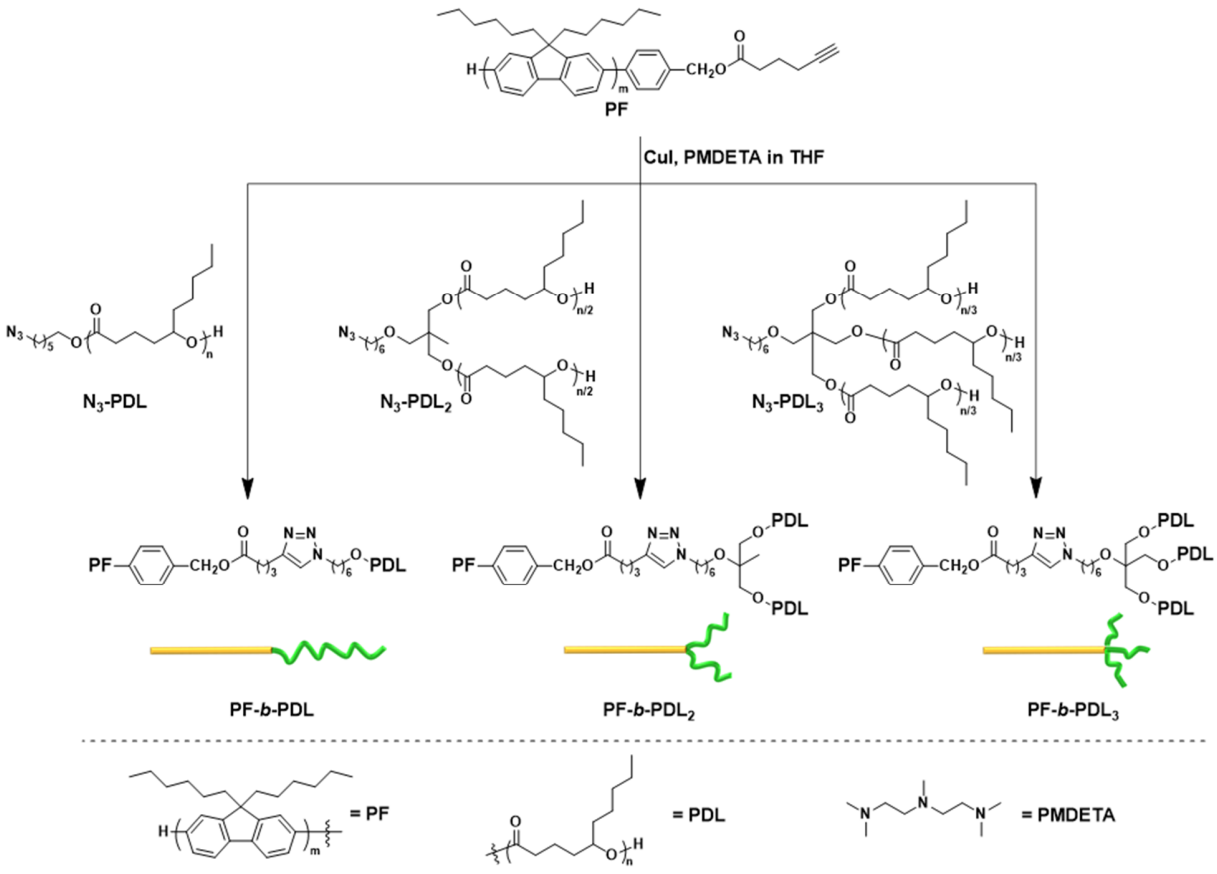

Scheme 1. Synthetic route for PF-*b*-PDL, PF-*b*-PDL_2, and PF-*b*-PDL_3 through CuAAC.

Polymer Characterization. Proton nuclear magnetic resonance (^{1}H NMR) spectra were recorded on a JEOL JNM-ECS400 400 MHz NMR spectrometer using deuterated chloroform. Size exclusion chromatography (SEC) measurements were performed at 40 °C using a Jasco GPC-900 system equipped with two Shodex KF-804L columns (8 mm × 300 mm) using THF as the eluent solvent at a flow rate of 1.0 mL·min^{-1}. Number-average molecular weight ($M_{n,SEC}$) and dispersity ($Đ$) of the polymers were calculated on the basis of a polystyrene standard. Fourier transform infrared spectroscopy (FTIR) measurements were performed using a PerkinElmer Frontier MIR spectrometer equipped with a single reflection diamond universal attenuated total reflection (ATR) accessory. Thermal gravimetric analysis (TGA) was conducted using a TA Instruments Q50 with a heating rate of 10 °C·min^{-1} from 100 °C to 650 °C under a flow of nitrogen. DSC measurements were conducted using a TA Instruments Q100 instrument in which 3-5 mg samples were measured with heating and cooling rates of 10 °C·min^{-1} between -70 °C and 235 °C.

Optical Properties, Electrical Properties, and Thin Film Morphology. Polymer thin films were prepared by spin-coating a polymer solution (3 g·L^{-1}) with a spin rate of 1000 rpm onto an ODTS-modified bare silicon wafer, quartz substrate, or indium tin oxide (ITO) glass. The ODTS-modified wafer was prepared by spin-coating a solution of ODTS in TCE (20 μL/20 mL, 3000 rpm) onto a UV-pretreated silicon wafer, followed by annealing with ammonia water for at least 24 h. The hydrophobic surface of the modified wafer facilitated the molecular packing and orientation of the polymer thin films.[32] The annealing process for the polymer thin films was carried out at 100 °C in a N_2-filled glovebox for 1 h. CV measurements was conducted with a CHI 627E electrochemical analyzer using a three-electrode cell system, with ITO glass used as the working electrode and a platinum wire as the auxiliary electrode. The Ag/AgCl, KCl (sat.) reference electrode was used to define the cell potential. Electrochemical properties of the polymer

films were measured using 0.1 M tetrabutylammonium perchlorate in anhydrous acetonitrile as the electrolyte. Solid-state UV-vis absorption spectra were recorded with a Hitachi U-4100 spectrophotometer. Nanostructures of the polymer thin films were visualized with AFM using a Nanoscope 3D controller atomic force microscope (Digital Instruments) operated in the tapping mode under an ambient atmosphere. The spring constant of the silicon cantilevers (Nanosensor PPP-SEIHR) was 15 N/m and the resonant frequency was 330 kHz. Grazing incidence wide angle X-ray scattering (GI-WAXS) measurements of the polymer films on ODTS-modified bare wafer substrates were conducted in the National Synchrotron Radiation Research Center in Taiwan (23A beamline) using an X-ray radiation source of $\lambda = 1.239851$ Å, and Pilatus 1M-F and C9728DK area detector. Cross-sectional Scanning Electron Microscope (SEM) images of the fabricated device were measured using a JSM-7600F Schottky Field Emission Scanning Electron Microscope. For the optical microscopy (OM) images of the stretched polymer films, films were first prepared on an ODTS-modified silicon wafer and then transferred to a cross-linked PDMS elastomeric substrate (reagent A:B = 20:1 (w/w)). The stretched polymer films were then transferred back to a second bare silicon wafer for the measurements, and the images were recorded using an OLYMPUS BX51 microscope.

Device Fabrication. Fabrication of n-type OFET memories with PTCDI-C8 as the semiconducting layer and the prepared PF-*b*-PDL$_x$ (x = 1-3) as the charge-storage layer (Si/SiO_2/PF-*b*-PDL$_x$/PTCDI-C8/Au) allowed us to investigate the charge-trapping properties of the prepared polymers. A 3 mg/mL solution of PF-*b*-PDL$_x$ in toluene was spin-coated onto the ODTS-modified SiO_2 (300 nm)/Si substrates at a spin rate of 1000 rpm. The average film thickness was 30-35 nm. The spin-casted polymer thin films were then thermally annealed at 100 °C for 1 h in a N_2-filled glovebox. Subsequently, 50 nm-thick PTCDI-C8 layer was thermally evaporated on

top of the polymer layer. 50 nm-thick gold source and drain electrodes were then subsequently thermally evaporated through a regular shadow mask with channel length (L) and width (W) of 50 and 1000 μm, respectively. For the OFET memories prepared from the stretched polymer thin films, the thermally annealed polymer thin films developed on the ODTS-modified SiO_2/Si substrates were first transferred to a PDMS substrate (reagent A:B = 20:1 (w/w)), and then the polymer films on PDMS substrates were stretched at different strain levels and clamped on a glass substrate. The polymer films were then transferred to a silicon wafer with a 300 nm SiO_2 layer. Finally, the PTCDI-C8 and gold electrodes were deposited in the same manner as the procedures mentioned above. Current-voltage characteristics (I_{ds}-V_g) of the fabricated OFETs were recorded in a N_2-filled glovebox using a Keithley 4200 semiconductor parametric analyzer (Keithley Instruments Inc., Cleveland, OH).

RESULTS AND DISCUSSION

Polymer Synthesis and Characterization. Molecular weight and $Đ$ values of the polymers used in this study are summarized in **Table 1**. Alkyne-PF and N_3-PDL$_x$ (x = 1-3) were prepared according to previous literature with precise molecular weight control; the corresponding ^{1}H NMR spectra are shown in **Figure S1** in the Supporting Information. The number-averaged molecular weight calculated from the ^{1}H NMR spectrum ($M_{n,NMR}$) of PF is 5400, and the $Đ$ value is 1.43. The $M_{n,NMR}$ values of N_3-PDL, N_3-PDL$_2$, and N_3-PDL$_3$ are 5100, 5000, and 5100, respectively, with $Đ$ values of 1.09, 1.13, and 1.14, respectively. Note that the number-averaged molecular weights calculated from the SEC traces ($M_{n,SEC}$) of N_3-PDL, N_3-PDL$_2$, and N_3-PDL$_3$ are 7200, 6600, and 6400, respectively. The lower $M_{n,SEC}$ of the branched PDLs indicates a smaller hydrodynamic volume. Since the PDL homopolymers exhibit nearly the same $M_{n,NMR}$ (5000-5100), it can be

concluded that the branched PDLs possess higher relative density compared with the linear PDL. A CuAAC click reaction was then performed between alkyne-PF and the N_3-PDL_x to obtain the desired BCPs. As shown in **Figure S2**, SEC traces of the BCPs clearly shift to higher molecular weight after the click reaction. The $M_{n,SEC}$ values of PF-*b*-PDL, PF-*b*-PDL_2, and PF-*b*-PDL_3 are 12800, 11700, and 11400, respectively. Compared with PF-*b*-PDL, the smaller $M_{n,SEC}$ values of PF-*b*-PDL_2 and PF-*b*-PDL_3 can be attributed to the smaller volume of the branched PDL building blocks. Moreover, $Đ$ values range from 1.41 to 1.46, showing that the molecular weight of the BCPs can be effectively controlled with our method. The chemical structures of the BCPs were then confirmed by FTIR spectroscopy and ^{1}H NMR spectroscopy. In the FTIR spectrum of PF-*b*-PDL (**Figure 1a**), an absorption band of the azido group from N_3-PDL at 2097 cm^{-1} completely disappears after the click reaction, indicating effective coupling between the alkyne and azido functional groups. Similar results were found for PF-*b*-PDL_2 and PF-*b*-PDL_3; the corresponding FTIR spectra are provided in **Figure S3**. ^{1}H NMR spectra of the BCPs (**Figure 1b**) possess the signals from both PF (0.59-1.12 ppm, 1.96-2.11 ppm, and 7.50-7.94 ppm) and PDL blocks (1.10-1.80 ppm, 2.11-2.22 ppm, and 4.79-4.91 ppm). The portion of PDL connected to polyfluorene (*%P*) was estimated using the integration of the ^{1}H NMR signal at 2.13 ppm (m, **PF** side chain -C-($CH_2C_5H_{11}$)$_2$) and 2.29 ppm (t, **PDL** main chain-COOC$H_2C_2H_4$CH) with the equation:

$$\%P = (A_{2.29} \div 2 \times N_{PDL}) \div [A_{2.13} \div 4 \times N_{PF}] \times 100\%,$$

where $A_{2.29}$ is intensity at 2.29 ppm, $A_{2.13}$ is intensity at 2.13 ppm, N_{PDL} is the number of repeat unit of PDL homopolymers, and N_{PF} is the number of repeat unit of PF homopolymer. The calculated *%P* values for the synthesis of PF-*b*-PDL, PF-*b*-PDL_2 and PF-*b*-PDL_3 are 94%, 93% and 97%, respectively, indicating satisfactory connection between PF and PDL segments. The combined results indicate that synthesis of the target BCPs with controlled molecular weight and block ratio

was successful. Note that the weight ratio of the PF block (w_{PF}) in all of the BCPs is controlled between 51.4% and 51.9% to assess the relationship between polymer architecture and polymer properties without any other effects originating from differences in the block ratios.

Table 1. Molecular weight parameters of the studied polymers.

Sample	$M_{n,NMR}$ [a]	$M_{n,SEC}$ [b]	$Đ$ [b]	w_{PF}
PF	5400	8600	1.43	100%
N_3-PDL	5100	7200	1.09	0%
N_3-PDL$_2$	5000	6600	1.13	0%
N_3-PDL$_3$	5100	6400	1.14	0%
PF-*b*-PDL	10500	12800	1.41	51.4%
PF-*b*-PDL$_2$	10400	11700	1.46	51.9%
PF-*b*-PDL$_3$	10500	11400	1.43	51.4%

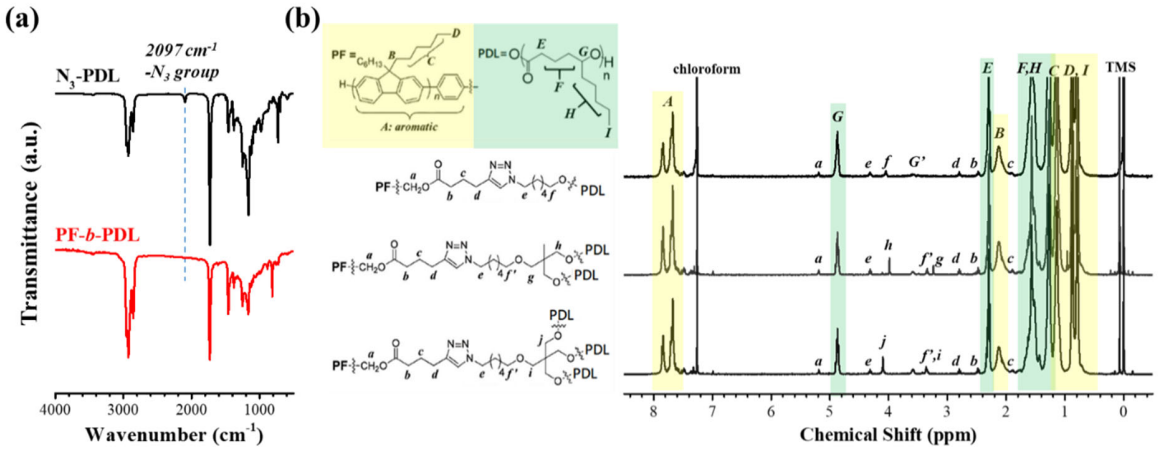

Figure 1. Characterizations of the BCPs. (a) FTIR spectra of N_3-PDL and PF-*b*-PDL. (b) ^{1}H NMR spectra (in $CDCl_3$) of PF-*b*-PDL, PF-*b*-PDL$_2$, and PF-*b*-PDL$_3$.

Thermal and Electrical Properties of PF and PF-based BCPs. Thermal and electrical properties of the polymers were investigated, and the results are summarized in **Table 2**, **Figure 2**, and **Figure 3**. Thermal stability of the BCPs was determined from TGA traces recorded from 100 °C to 650 °C (**Figure S4**). The BCPs exhibit two degradation temperatures ($T_{d,\,5\%}$), at 290.2-297.1 °C and 375.0-380.8 °C, which represent the 5% degradation of the PDL block and the PF block, respectively. DSC measurements with a ramp rate of 10 °C/min under nitrogen flow were performed to investigate phase transitions of the studied polymers (**Figure 2**). The DSC traces were recorded at temperatures up to 235 °C to prevent thermal decomposition of the PDL segments.

Table 2. Thermal and electrical properties of alkyne-PF, PF-*b*-PDL, PF-*b*-PDL$_2$, and PF-*b*-PDL$_3$.

Sample	**ΔH_c** [a] **(J/g)**	**FWHM$_c$** [a] **(°C)**	**ΔH_m** [b] **(J/g)**	**HOMO** [c] **(eV)**	**LUMO** [d] **(eV)**
alkyne-PF	-	-	-	-5.63	-2.73
PF-*b*-PDL	5.68	15.5	5.88	-5.63	-2.73
PF-*b*-PDL$_2$	6.83	14.6	7.04	-5.61	-2.71
PF-*b*-PDL$_3$	8.98	14.4	9.29	-5.61	-2.71

[a] Calculated from DSC first cooling curves. [b] Calculated from DSC second heating curves. [c] Calculated from the onset oxidation potential measured by CV. [d] Calculated using the formula LUMO = HOMO + E_g. E_g was determined from the onset UV absorption of the annealed polymer films.

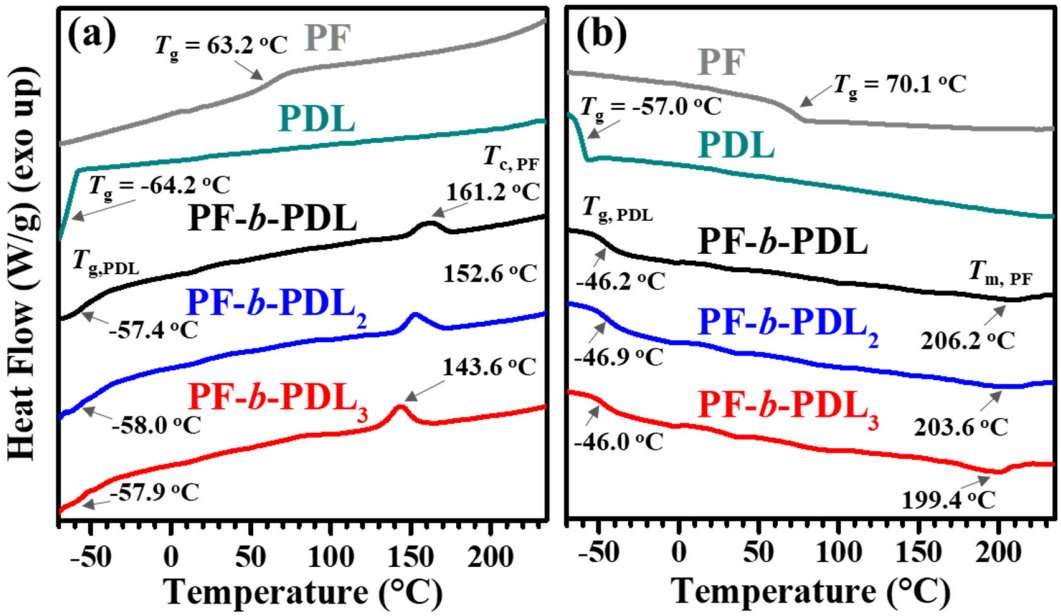

Figure 2. DSC (a) first cooling and (b) second heating curves of alkyne-PF (PF), N_3-PDL (PDL), PF-*b*-PDL, PF-*b*-PDL_2, and PF-*b*-PDL_3.

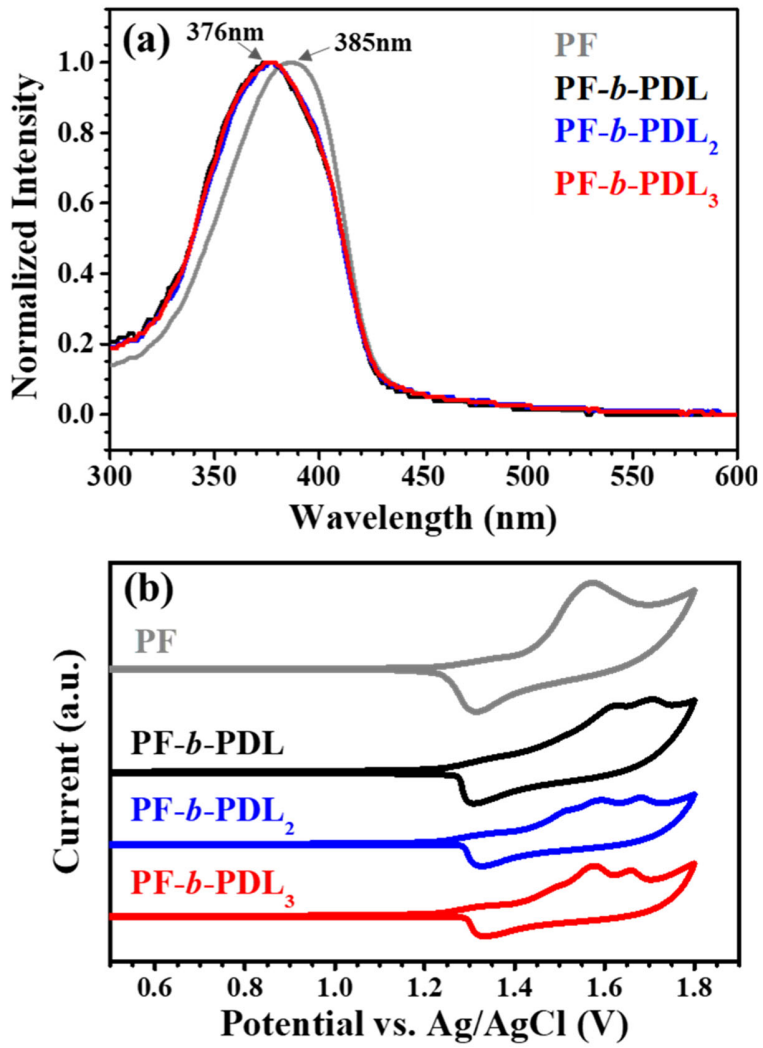

Figure 3. (a) UV-vis absorption spectra and (b) CV curves of the annealed polymer thin films (annealing conditions: 100 °C, 1 h).

The PF homopolymers (alkyne-PF) exhibits a significant glass transition temperature (T_g) at 63.2 °C in the first cooling curve (**Figure 2a**) and at 70.1 °C in the second heating curve (**Figure 2b**). No melting or crystallization peaks were identified in the cooling and heating curves, suggesting low crystallinity of the PF homopolymer. Compared with a previous report on poly(9,9-di-*n*-hexyl-2,7-fluorene) with a molecular weight of 45000 that exhibited high crystallinity,[37] the

poor crystallinity of our PF homopolymer can be explained by the low molecular weight of the sample. The PDL homopolymer (represented by N_3-PDL) exhibits a T_g at -64.2 °C in the first cooling curve and at -57.0 °C in the second heating curve, demonstrating the benefit of PDL as a soft building block of the BCP. All of the BCPs exhibit glass transition temperatures that vary between -58.0 °C and -57.4 °C during the first cooling, and between -46.9 °C and -46.0 °C during the second heating, representing the glass transition temperature of the PDL segments in the BCPs ($T_{g,PDL}$). Conversely, the glass transition temperature of the PF segment is indistinguishable among all of the BCP samples. Instead of exhibiting a T_g of the PF segment, each BCP sample exhibits a sharp exothermic peak (143.6-161.2 °C) during the first cooling, and a broader endothermic peak (199.4-206.2 °C) during the second heating. These phase transitions can be regarded as the crystallization process and melting process of the PF crystalline phase, respectively.[37] This suggests that the PDL segments in our BCP system facilitate the crystallization process of the PF segment, which originally exhibits poor crystallinity as the homopolymer. Moreover, the much lower crystallization temperature ($T_{c,PF}$, **Figure 2a**) of the branched BCPs can be attributed to the confined crystallization and homogeneous nucleation of the polymer.[38] Note that the crystalline structure of the PF segments in the BCPs was confirmed as the α crystalline form of poly(9,9-di-*n*-hexyl-2,7-fluorene)[37] by grazing-incidence wide-angle X-ray scattering (GI-WAXS) measurements, which will be discussed in the next section.

To investigate the kinetics of the crystallization process in more detail, the enthalpy of crystallization (ΔH_c), enthalpy of fusion (ΔH_m), and full width at half-maximum of crystallization ($FWHM_c$) were calculated and are summarized in **Table 2**. The ΔH_c and ΔH_m were calculated considering the composition of the PF segment in each BCP sample. As shown in **Table 2**, ΔH_c and ΔH_m of the BCPs gradually increase as the branching number increases, indicating higher

crystallinity of the branched BCPs. Moreover, the smaller $FWHM_c$ of the branched BCPs can be attributed to smaller crystal size distribution.[39-40] Based on the DSC studies, it can be inferred that the PF segments in the branched BCPs may undergo a more homogeneous crystallization process, leading to higher crystallinity and a more uniform PF crystalline phase.

The electronic properties of alkyne-PF (denoted as PF), PF-*b*-PDL, PF-*b*-PDL_2, and PF-*b*-PDL_3 were studied by UV-vis absorption and CV of the annealed polymer thin films. The as-cast polymer thin films possess one absorption band with the same peak at 385 nm (**Figure S5**). After thermal annealing **(Figure 3a**), all of the BCPs exhibit a blue-shift of absorption to 376 nm, whereas the absorption band of the PF homopolymer remains unchanged. This finding is in agreement with a previous report on poly(9,9-di-*n*-hexyl-2,7-fluorene),[41] in which a blue-shift of the UV absorption peak was observed in conjunction with the growth of α crystallites in the melt-quenched polyfluorene sample. To compare the energy levels of the PF homopolymer and the BCPs, the optical band gap (E_g) was calculated from the onset absorption of the annealed films (**Figure 3a**), and CV measurements (**Figure 3b**) were conducted to determine the exact HOMO level. The LUMO level was then calculated from the equation LUMO = HOMO + E_g. The HOMO/LUMO values of PF, PF-*b*-PDL, PF-*b*-PDL_2, and PF-*b*-PDL_3 are -5.63/-2.73, -5.63/-2.73, -5.61/-2.71, and -5.61/-2.71 eV, respectively (summarized in **Table 2**). This demonstrates that incorporation of the soft PDL segments does not affect the energy levels of the semiconducting polymer, as expected.

Thin Film Morphologies and the Features of Polyfluorene Nanofibers. The branched PDL soft segments are expected to modulate the phase separation of BCP and facilitate crystallization of the PF segment. Thin film morphology of the annealed polymer films (30 nm thick) was investigated by AFM and GI-WAXS experiments. To extract the features of the PF nanofibers

from the AFM phase images of the BCPs, the nanofibers were identified using GTFiber software;[42] this is the first time that this method has been applied to a conjugated BCP system. In the phase images of the PF homopolymer (**Figure S6b**), no distinct phase-separated structure was observed, owing to the continuous PF domain within the polymer film. Conversely, the phase image of the PF-*b*-PDL film (**Figure 4a**) exhibits distinguishable soft (dark) and hard (bright) domains, in which the bright stripes are the nanofibrous structures formed by the assembly of PF. Moreover, the phase images of the branched polymers, PF-*b*-PDL$_2$ (**Figure 4b**) and PF-*b*-PDL$_3$ (**Figure 4c**), exhibit higher contrast and longer nanofibrous structures. The longer PF nanofibers in the branched BCP samples are likely due to the confined crystallization and homogeneous nucleation of the PF segment, as explained by the lower $T_{c,\,PF}$ and smaller FWHM$_c$ in the DSC studies. AFM height images of the studied polymers are provided in **Figure S6a** and **S6c-e**, with root-mean-square surface roughness (R_q) of alkyne-PF, PF-*b*-PDL, PF-*b*-PDL$_2$, and PF-*b*-PDL$_3$ calculated from the image as 0.76, 3.85, 4.16, and 3.75 nm, respectively. The slightly higher R_q of the BCP films arises from the phase separation of the BCPs.

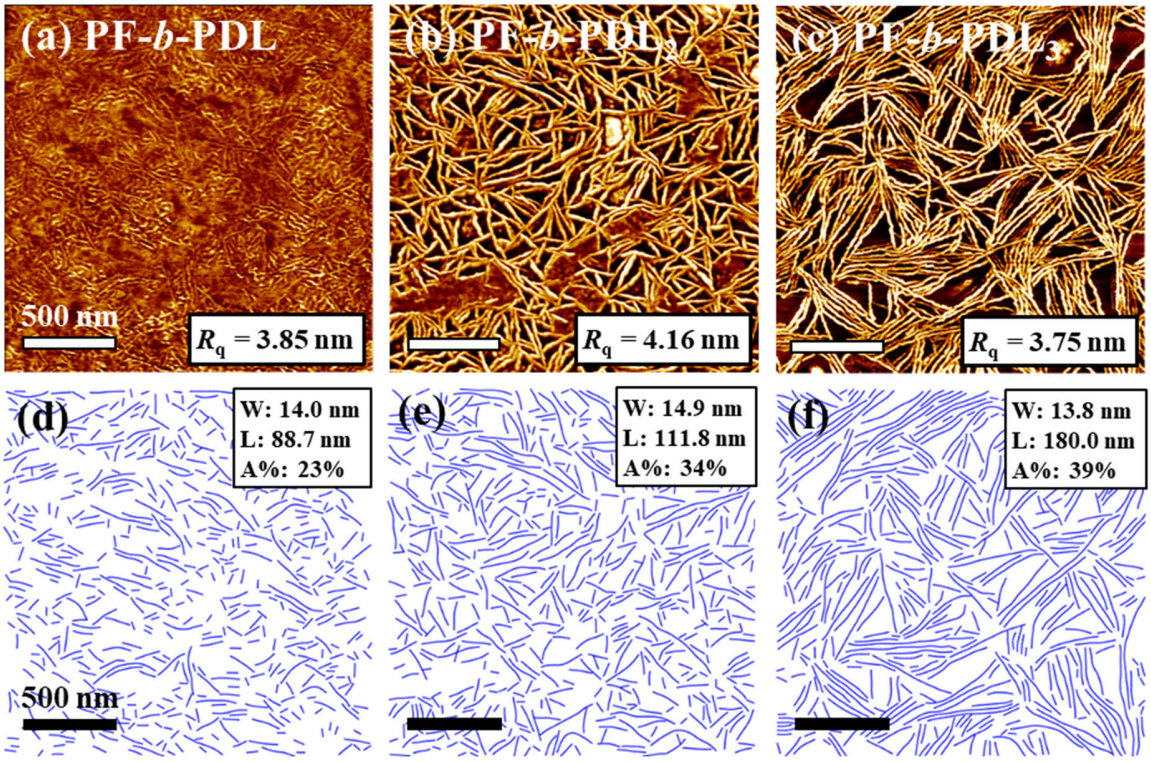

Figure 4. (a-c) AFM phase images and (d-f) the corresponding identified fiber images of (a, d) PF-*b*-PDL, (b, e) PF-*b*-PDL$_2$, and (c, f) PF-*b*-PDL$_3$. The insets of Figure 4d-4f show the average width (W), length (L), and coverage area (A%) of the polyfluorene nanofibers.

AFM measurements frequently yield images with low contrast and moderate noise, thus making it difficult to extract features of the nanofibers from images.[42] Therefore, the identified fiber images, in which the nanofibers were identified from AFM images and thinned to single-pixel width, are more suitable choices for quantitative analysis. **Figure 4d-f** show the identified fiber images of the BCPs and the features of the PF nanofibers (width (W), length (L), and coverage area (A%)). The parameters used for identification of the fibers are provided in **Figure S7** to aid readers in obtaining the same fiber images from our AFM images. As shown in Figure 4d-f, all of the BCP samples exhibit PF nanofibers with similar fiber widths (W = 13.8-14.9 nm). However, the length

of the nanofibers varies with the polymer architecture. The average length of the nanofibers in the PF-*b*-PDL, PF-*b*-PDL$_2$, and PF-*b*-PDL$_3$ films is 88.7 nm, 111.8 nm, and 180.0 nm, respectively, revealing that the branched PDL segments in the BCPs benefit the formation of long-range crystalline structures of PF. Aside from the width and length of the PF nanofibers, we are particularly interested in the coverage area (A%) of PF nanofibers on the polymer thin films. Since the confined PF crystalline domains in the insulating polymer (PDL) matrix can be regarded as effective hole-trapping sites,[30] the A% value can be correlated with the hole trapping density of the polymer electret. The A% value is calculated from the single-pixel width fiber images (**Figure 4d-f**) considering the average width of the nanofibers. As shown in **Figure 4d-f**, the A% values of PF-*b*-PDL, PF-*b*-PDL$_2$, and PF-*b*-PDL$_3$ are 23%, 34%, and 39%, respectively. The larger A% value of the branched BCPs (PF-*b*-PDL$_2$ and PF-*b*-PDL$_3$) can be attributed to two main reasons: 1) stronger phase separation behavior and higher crystallinity (supported by DSC data) of the branched BCPs, leading to more distinct and confined PF domains; and 2) higher relative density and smaller volume of the branched PDL segments, as evidenced by the SEC traces, which result in a higher volume ratio of PF in the branched BCPs. Quantitative analysis of the PF nanofibrous structure indicates that the branched BCPs as a charge-storage layer may provide more charge trapping sites for memory devices. The A% are listed in **Table 3** with the OFET device performance, which will be discussed in the next section.

Table 3. Coverage area of polyfluorene nanofibers (A%) and OFET memory performance of the studied polymer electrets.

Polymer	A [a] (%)	μ_{ave} ($cm^2V^{-1}S^{-1}$)	I_{on}/I_{off} (-)	V_{th} (V)			ΔV_{th} (V)	I_{write}/I_{erase} (-)	Δn (cm^{-2})
				Initial	*Writing*	*Erasing*			
PF	-	7.1×10^{-2}	2.3×10^{5}	32	*-43	*35	*78	$*1.9\times10^{5}$	$*5.6\times10^{12}$
PF-*b*-PDL	23	1.3×10^{-2}	9.5×10^{3}	24	-32	31	63	4.1×10^{3}	4.5×10^{12}
PF-*b*-PDL$_2$	34	1.1×10^{-2}	2.9×10^{4}	23	-56	30	86	2.4×10^{4}	6.2×10^{12}
PF-*b*-PDL$_3$	39	1.0×10^{-2}	1.0×10^{5}	23	-70	32	102	3.5×10^{4}	7.3×10^{12}

[a] Determined from the identified fiber images of the BCPs (**Figure 4d-f**).

* The PF homopolymer device exhibits transient memory behavior with poor on-current retention, as shown in **Figure 6c**.

GI-WAXS measurements were conducted to better understand the molecular packing within the polymer thin films. As shown in **Figure 5a**, no distinguishable scattering patterns were present in the GI-WAXS two-dimensional (2D) image of alkyne-PF as a result of poor crystallinity of the PF homopolymer. Interestingly, the GI-WAXS 2D images of PF-*b*-PDL, PF-*b*-PDL$_2$, and PF-*b*-PDL$_3$ (**Figure 5b-d**) exhibit multiple scattering spots with almost the same q values. Furthermore, the BCP samples each exhibit a scattering spot with the highest intensity in the out-of-plane (q_z) direction (q = 0.564 $Å^{-1}$, d = 11.1 Å). According to the X-ray diffraction data of poly(9,9-di-*n*-hexyl-2,7-fluorene),[37] this scattering spot represents the characteristic lamellar reflection (200) of the α crystallites. Therefore, it can be concluded that the PF block of our BCPs form α phase crystallites, with stacking of the lamellar structure perpendicular to the surface of the silicon wafer

substrate. Moreover, the scattering patterns clearly indicate an orthogonal unit cell (a = 2.23 nm, b = 2.37 nm, c = 3.23 nm), in which a is along the q_z direction, and b and c are along the q_{xy} direction. This type of GI-WAXS pattern has been reported for the melt-crystallized α phase nanofibril films of monodisperse poly(9,9-di-*n*-octyl-2,7-fluorene) (PFO),[43] but has never been reported for any studies involving poly(9,9-di-*n*-hexyl-2,7-fluorene)-based polymers. We speculate that the incorporated soft PDL segments in the BCPs facilitate the assembly of the PF block through phase separation, thus leading to highly oriented α crystallites of PF within the PF nanofibers.

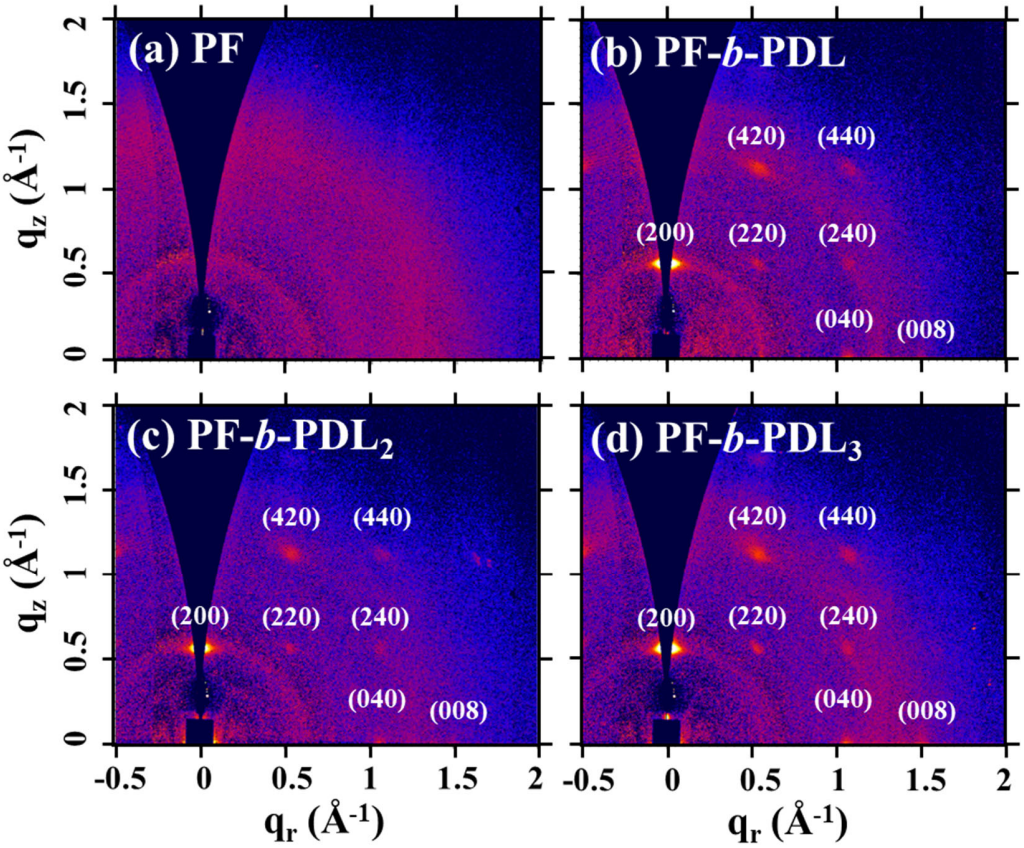

Figure 5. GI-WAXS 2D images of (a) alkyne-PF (PF), (b) PF-*b*-PDL, (c) PF-*b*-PDL$_2$, and (d) PF-*b*-PDL$_3$.

OFET Memories with PF-*b*-PDLs as Charge-Storage Layer. OFET memories with different polymer electrets (Si/SiO_2 (300 nm)/PF or PF-*b*-PDL_x/PTCDI-C8/Au) were fabricated and the device performance was investigated, as summarized in **Table 3**. The cross-sectional SEM image of the PF-*b*-PDL_3 device is provided in **Figure S8**. Note that PTCDI-C8 was chosen as n-type semiconducting layer for the fabrication of OFET device. Due to the built-in electric field formed by the holes trapped in the PF-based polymer electret, electrons can be more easily accumulated at the semiconductor/electret interface, facilitating the transportation of electrons in the PTCDI-C8 layer. Therefore, the drain current-gate voltage (I_{ds}-V_g) curve shows a negative shift and the device could retain at high conductive state even when the gate bias is removed. Also, the HOMO and LUMO energy levels of PTCDI-C8 are -6.3 eV and -4.3 eV, respectively.[44] The holes injected to the polymer electret layer could be stabilized owing to the sufficiently low HOMO level of PTCDI-C8 compared with the prepared PF-based BCPs (-5.63 to -5.61 eV).

All of the devices were measured in the dark to avoid light-induced charge transfer or excitons in the charge-storage and semiconducting layers. Judging from the initial I_{ds}-V_g curves (**Figure S9a**), the average charge mobility of the OFET memories (μ_{ave}) with electrets of PF, PF-*b*-PDL, PF-*b*-PDL_2, and PF-*b*-PDL_3 is 7.1×10^{-2}, 1.3×10^{-2}, 1.1×10^{-2}, and 1.0×10^{-2} $cm^2V^{-1}S^{-1}$, respectively, and the on/off current ratio (I_{on}/I_{off}) of the devices ranges from 9.5×10^3 to 2.3×10^5, respectively. The PF homopolymer device exhibits comparable mobility with the PTCDI-C8 OFET (Si/SiO_2/PTCDI-C8/Au) (**Figure S9b**). Due to more hydrophilic surface (contact angle measurements, **Figure S10**), and higher surface roughness of the BCP electrets, the subsequently deposited PTCDI-C8 layer exhibit smaller grain size and higher surface roughness as investigated by AFM (**Fig. S11**). Therefore, the devices of BCP electrets possess slightly lower charge mobility of the BCP devices compared with the PF-based device.

After applying a gate voltage (V_g) of -140 V for 8 s as the "writing" process (**Figure 6a**), the PF and BCP devices turn to the ON state and the transfer curves shift in the negative direction, leading to much higher drain current at $V_g = 0$. The "erasing" process was performed by applying a V_g of 140 V for 2 s, resulting in a backward shift of the transfer curves to the OFF state along with a slightly more positive threshold voltage (V_{th}) than the initial state. The slightly lower V_{th} of the initial curve than the erasing curve of each OFET memory is due to the small number of holes trapped in the film before OFET operation. The memory window (ΔV_{th}) of the PF, PF-*b*-PDL, PF-*b*-PDL$_2$, and PF-*b*-PDL$_3$ devices is 78, 63, 86, and 102 V, respectively, and the memory ratio (I_{write}/I_{erase}) at $V_g = 0$ is 1.9×10^5, 4.1×10^3, 2.4×10^4, and 3.5×10^4, respectively, indicating that the memory behavior of the devices can be modulated through the choice of polymer electret. The drain current retention of the device at the ON and OFF states was recorded at $V_g = 0$ and $V_d = 80$ V (**Figure 6b**). Although the PF homopolymer device exhibits a large memory window of 78 V, the drain current of the ON state drops to a similar level as that of the OFF state (10^{-11} A) after 4000 s due to the continuous PF domain in the electret that forces charges to rapidly dissipate.[30] On the contrary, the drain current of the BCP devices in the ON state decreases more slowly, reaching a steady value after 10000 s, which is at least two orders of magnitude higher than the OFF state. This demonstrates that it is beneficial to employ a conjugated/insulating BCP as the electret for non-volatile OFET memory. Moreover, the drain current of the PF-*b*-PDL, PF-*b*-PDL$_2$, and PF-*b*-PDL$_3$ devices in the ON state after 10000 s is 1.1×10^{-9}, 8.3×10^{-8}, and 4.5×10^{-7} A, respectively, revealing superior memory performance of the branched BCP devices compared to the linear BCP device.

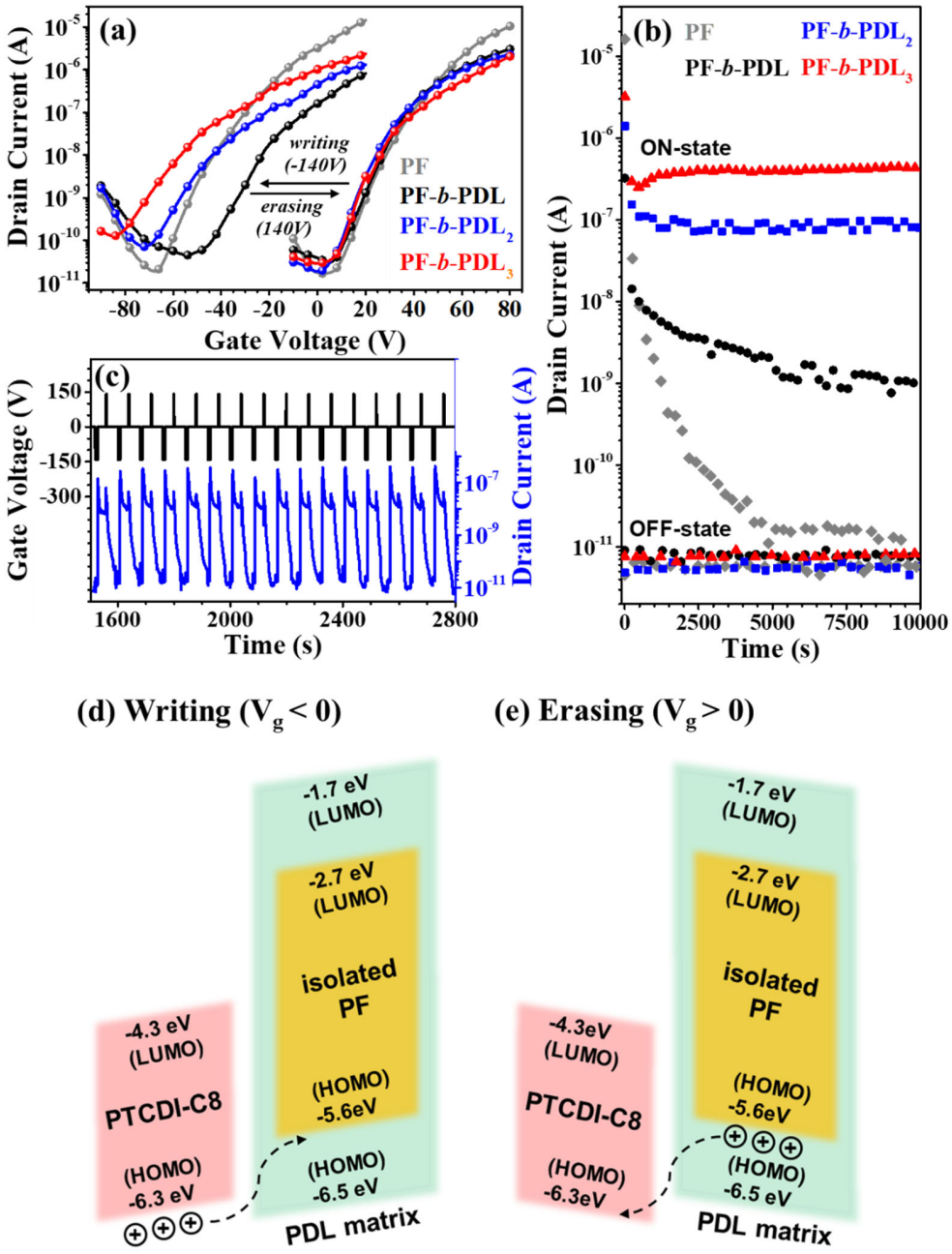

Figure 6. (a) Writing/erasing plots and (b) corresponding memory retention characteristics (V_g = 0V) of the OFET devices at V_d = 80 V. (c) WRER cycles of the PF-*b*-PDL3 device at V_d = 80 V. Proposed mechanism and energy band diagrams under the (d) negative and (e) positive gate voltage bias for the OFET memory using the block copolymers as polymer electrets.

Trapping density (Δn) of the memory devices was then calculated from the equation $\Delta n = (\Delta V_{th}/e) \times C$, where ΔV_{th} is the memory window, e is the charge of a hole, and C is the capacitance. As shown in Table 3, Δn can be effectively improved from 4.5×10^{12} (PF-*b*-PDL) to 7.3×10^{12} (PF-*b*-PDL$_3$) by increasing the branching number of the PDL segments, which can be comprehensively explained by the higher A% value of the branched BCP thin films. The rewritability of the OFET memories of BCP was than examined with write-read-erase-read (WRER) cycles at V_g = 140 V (8 s), 0 V (30 s), -140 V (2 s), and 0 V (40 s). As can be seen in **Figure 6c**, the PF-*b*-PDL$_3$ device can be repeatedly written and erased with an ON/OFF current ratio > 10^3. The PF-*b*-PDL and PF-*b*-PDL$_2$ devices also retain their performance after WRER cycles, but they exhibit slightly lower ON/OFF ratios due to the presence of fewer charge-trapping sites within the charge-storage layer (**Figure S12**).

The proposed operating mechanism and energy band diagrams of the OFET memories with PF-*b*-PDL$_x$ as electrets were shown in **Figure 6d** and **6e**. Energy levels of the insulating PDL matrix (represented by N$_3$-PDL) were calculated from UV (**Figure S13a**) and CV (**Figure S13b**) measurements to better understand the mechanism. The calculated HOMO and LUMO levels of the PDL matrix are -6.5 and -1.7 eV, respectively. During the writing process (**Figure 6d**), a large number of holes were induced in the HOMO level (-6.3 eV) of PTCDI-C8, and those holes were tunneled and stabilized into the isolated PF domain. Due to the sufficiently high HOMO level of PF (-5.7 eV) and the energy barrier from the low-lying HOMO level of PDL (-6.5 eV), the injected holes can be retained in the PF domain even after removing the gate bias, leading to a non-volatile memory-performing device. During the erasing process (**Figure 6e**), the holes in the PF domain were tunneled back to the PTCDI-C8 layer due to the repulsive force created from the positive gate bias, thus the device can be turned back to the OFF state. Collectively, the energy level

adaptation between PTCDI-C8 and the BCPs conduces to a respectable, reproducible and rewritable device performance. To verify that our polymer electrets can be applied for low-voltage -driven devices, we fabricated the OFET memories of PF-*b*-PDL and PF-*b*-PDL$_3$ on top of silicon wafers with 100nm SiO_2 dielectric layer (Si/SiO_2 (100nm)/PF-*b*-PDL$_x$/PTCDI-C8/Au). As shown in **Figure S14**, owing to lower capacitance of 100-nm SiO_2, the memory devices can be operated with the writing/erasing gate bias at ± 40V, and be read at V_d = 30V with favorable ΔV_{th} and I_{write}/I_{erase} values.

Stretchability of Polymer Thin Films and Stretchable Device Applications. Finally, we examined the stretchability of the polymer thin films from OM images and then fabricated the OFET memories with the stretched and transferred polymer electret films. As shown in **Figure 7**, the PF homopolymer thin film cannot endure the applied strain, exhibiting obvious cracks perpendicular to the strain direction at 25% strain, which grow even larger at higher stretching loadings. On the other hand, all of the BCP thin films exhibit favorable stretchability due to incorporation of the soft PDL segments, which do not crack at up to 100% strain. This suggests that our BCPs are suitable for use in stretchable electronic devices.

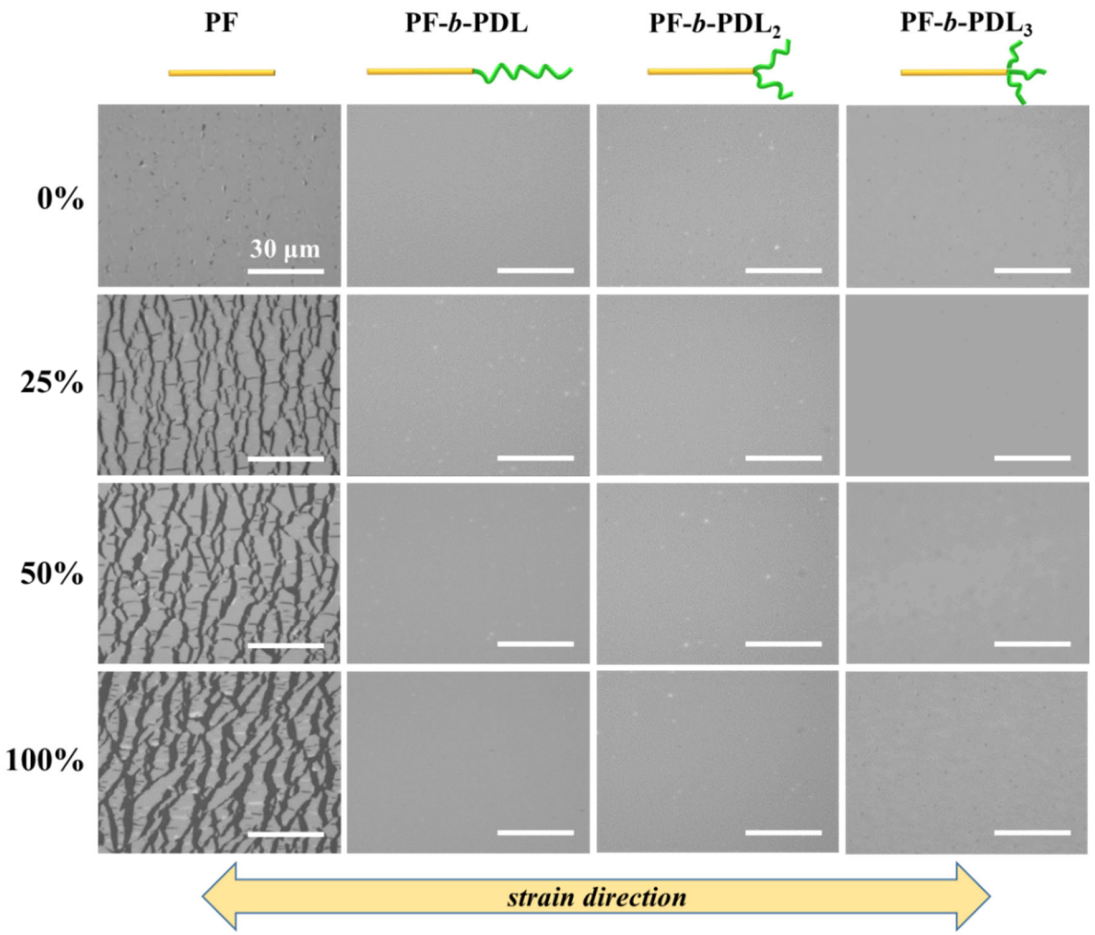

Figure 7. OM images of the stretched polymer thin films. The annealed polymer films were transferred from an ODTS wafer to a PDMS substrate, stretched at different loadings, and transferred back to a second bare silicon wafer for the measurements.

The structure of the OFET memories of the stretched and transferred BCP electrets is illustrated in **Figure 8a**. The performance of the BCP electrets under different strain loadings was compared by analyzing the I_{ds}-V_g curves of the ON and OFF states of the devices. PF-based device (**Figure 8b**) shows deteriorated performance from 50% of strain, which is result from the micrometer-scale cracks formed on the electret layer that affect the smoothness and uniformity of the subsequently

deposited PTCDI-C8 layer. Unlike the PF-based device, the BCP devices (**Figure 8c-e**) can be written and erased at up to 100% strain without a significant change in V_{th} in the ON and OFF states. As shown in **Figure 8f** (dashed lines), the mobility retention of all the BCP devices is > 50% after applying 100% strain. Note that the on-current and mobility of the devices with 0% strain in Fig. 8b-e is lower than those of the devices in Fig. 6a. It is due to the defects formed at the SiO_2 dielectric/polymer interface during the film transferring process.[32] The memory window of the BCP devices (**Figure 8f**, solid lines) drops slightly before reaching 50% strain, and then becomes steady at higher stretching loadings. Our results indicate that the prepared conjugated/insulating BCPs perform well as stretchable hole-trapping materials. Furthermore, the PF-*b*-PDL_3 device exhibits a memory window of 90 V (91% retention) at 100% strain, demonstrating extraordinary memory performance of the stretchable device. Finally, I_{ds}-V_g curves of the PF-*b*-PDL_3 device after 0-500 stretch-release cycles at 50% strain were recorded (**Figure S15**) and the device performance was evaluated. As shown in **Figure 8g**, charge mobility of the PF-*b*-PDL_3 device drops within one order of magnitude (34% mobility retention), and the memory window of the device changes from 99 V to 83 V (84% memory window retention) after 500 cycles, demonstrating excellent durability of the device under strain. The performance of the stretchable devices is summarized in **Table S1**.

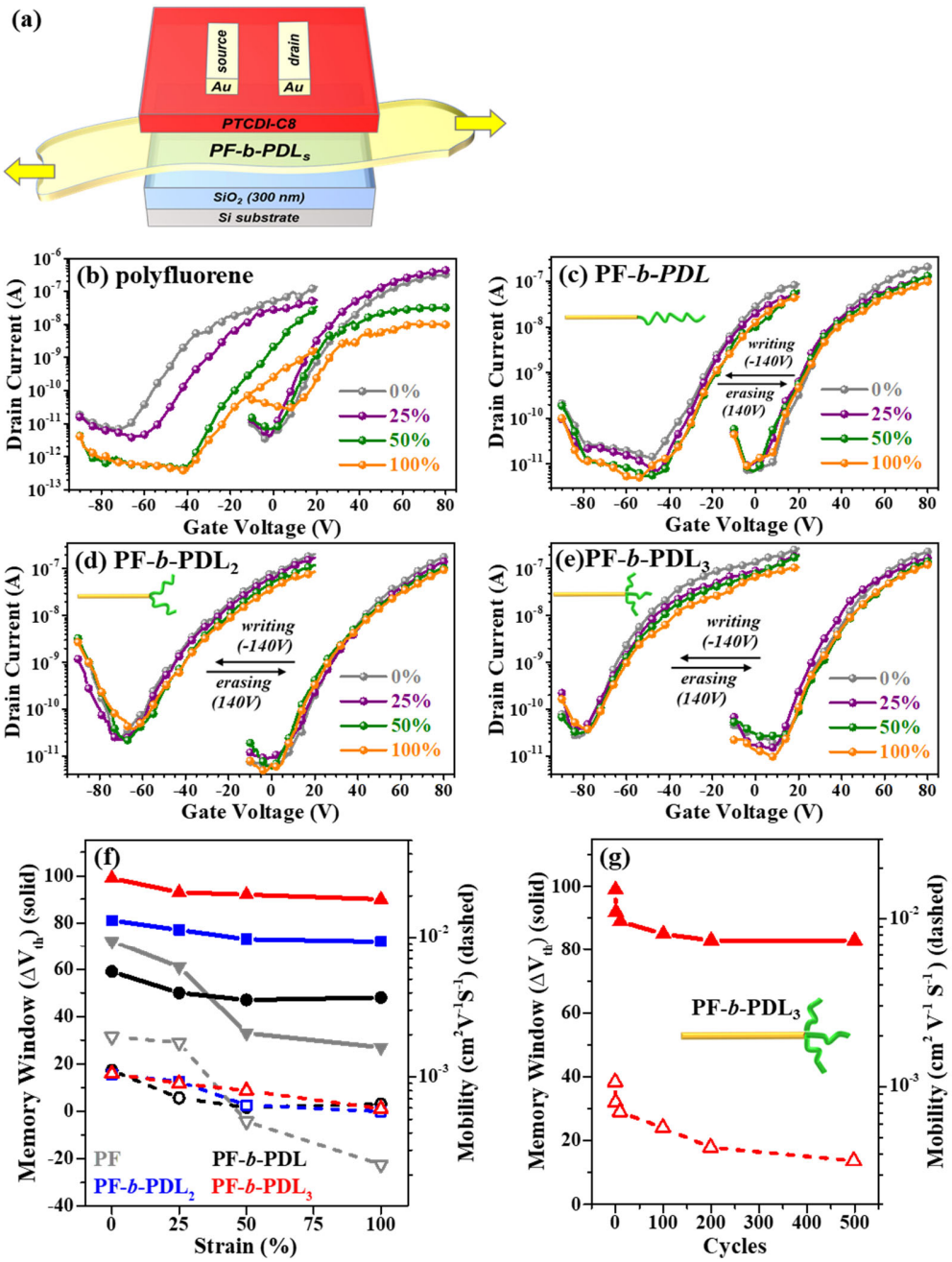

Figure 8. (a) Structure of the stretchable OFET memories. Writing/erasing plots of the OFET memories made from the stretched and transferred (b) PF, (c) PF-*b*-PDL, (d) PF-*b*-PDL$_2$, and (e) PF-*b*-PDL$_3$ films at V_d = 80 V. (f) Memory window (solid lines) and charge mobility (dashed lines) of the stretchable memory device. (g) Memory window (solid lines) and charge mobility (dashed lines) of the PF-*b*-PDL$_3$ device after stretch-release cycles at 50% strain. (V_d = 80 V).

CONCLUSION

We synthesized poly(9,9-di-*n*-hexyl-2,7-fluorene)-*block*-poly(*δ*-decanolactone) (PF-*b*-PDL) with AB, AB_2, and AB_3 architectures for OFET memory applications. Judging from the DSC data, the PF block of the branched BCPs underwent a more homogeneous crystallization process than the linear BCP, leading to higher PF crystallinity and a more uniform PF crystalline phase. In the thin film state, the annealed BCP thin films formed nanofibrous structures of PF with highly oriented α crystallites on silicon wafer substrates owing to the incorporated PDL segments. Moreover, the average fiber width, length, and coverage area of the PF nanofibers on the thin films were quantitatively analyzed using AFM phase images. The results indicate that the BCPs with branched PDL segments form longer PF nanofibers with a larger coverage area, which is desirable for memory device applications. Consequently, the OFET memory with the charge-storage layer of PF-*b*-PDL_3 exhibited the largest memory window (102 V), highest memory ratio (3.5×10^4), and highest hole-trapping density (7.3×10^{12} cm^{-2}). Stretchable OFET devices were fabricated, with all of the BCP devices retaining their performance at up to 100% strain. In particular, exposing PF-*b*-PDL_3 to 500 stretch-release cycles at 50% strain resulted in 34% mobility retention and 84% memory window retention. This study provides a new strategy to create high-performance and stretchable hole-trapping materials through the design of conjugated/insulating block copolymer architectures, thus demonstrating a new protocol that correlates the morphology of BCP films with memory device performance.

ASSOCIATED CONTENT

Supporting Information

Detailed synthetic procedures for the studied polymers, ^{1}H NMR spectra, SEC traces, FTIR spectra, TGA traces, additional UV-vis absorption spectra, additional AFM images, additional GI-WAXS data, contact angle measurements, and additional OFET characteristics of the studied polymers.

AUTHOR INFORMATION

Corresponding Author

*Toshifumi Satoh - Faculty of Engineering, Hokkaido University, Sapporo 060-8628, Japan; Email: satoh@eng.hokudai.ac.jp

* Wen-Chang Chen - Department of Chemical Engineering and Advanced Research Center for Green Materials Science and Technology, National Taiwan University, Taipei 10617, Taiwan; Email: chenwc@ntu.edu.tw

Author Contributions

The manuscript was written through contributions of all authors. All authors have given approval to the final version of the manuscript.

Notes

The authors declare no competing financial interest.

ACKNOWLEDGMENT

The authors appreciate the financial support by the Advanced Research Center for Green Materials Science and Technology from the Featured Area Research Center Program within the framework of the Higher Education Sprout Project by the Ministry of Education (grant no. 108L9006) and the Ministry of Science and Technology in Taiwan (grant no. MOST 108-3017-F-002-002). Research performed at Hokkaido University was financially supported by the JSPS KAKENHI Hybrid Catalysis for Enabling Molecular Synthesis on Demand initiative (grant nos. 19H02769 and JP20H04798), JST CREST (grant no. JPMJCR19T4), Frontier Chemistry Center (Hokkaido University), and the Photo-excitonix Project (Hokkaido University). The authors also acknowledge the National Synchrotron Radiation Research Center (NSRRC), Taiwan for facilitating the GI-WAXS experiments. We also thank to Ms. S.-J. Ji of Ministry of Science and Technology (National Taiwan University) for the assistance in cross-sectional SEM experiments.

REFERENCES

(1) Qian, Y.; Zhang, X.; Xie, L.; Qi, D.; Chandran, B. K.; Chen, X.; Huang, W., Stretchable Organic Semiconductor Devices. *Adv. Mater.* **2016**, *28*, 9243-9265.
(2) Trung, T. Q.; Lee, N. E., Recent Progress on Stretchable Electronic Devices with Intrinsically Stretchable Components. *Adv. Mater.* **2017**, *29*, 1603167.
(3) Wang, G. J. N.; Gasperini, A.; Bao, Z., Stretchable Polymer Semiconductors for Plastic Electronics. *Adv. Electron. Mater.* **2018**, *4*, 1700429.
(4) Rim, Y. S.; Bae, S. H.; Chen, H.; De Marco, N.; Yang, Y., Recent Progress in Materials and Devices toward Printable and Flexible Sensors. *Adv. Mater.* **2016**, *28*, 4415-4440.
(5) Boutry, C. M.; Kaizawa, Y.; Schroeder, B. C.; Chortos, A.; Legrand, A.; Wang, Z.; Chang, J.; Fox, P.; Bao, Z., A Stretchable and Biodegradable Strain and Pressure Sensor for Orthopaedic Application. *Nature Electronics* **2018**, *1*, 314-321.
(6) Wu, J.; Wu, Z.; Xu, H.; Wu, Q.; Liu, C.; Yang, B.-R.; Gui, X.; Xie, X.; Tao, K.; Shen, Y., An Intrinsically Stretchable Humidity Sensor Based on Anti-drying, Self-healing and Transparent Organohydrogels. *Materials Horizons* **2019**, *6*, 595-603.
(7) Ashizawa, M.; Zheng, Y.; Tran, H.; Bao, Z., Intrinsically Stretchable Conjugated Polymer Semiconductors in Field Effect Transistors. *Prog. Polym. Sci.* **2019**, *100*, 101181.
(8) Oh, J. Y.; Rondeau-Gagné, S.; Chiu, Y.-C.; Chortos, A.; Lissel, F.; Wang, G.-J. N.; Schroeder, B. C.; Kurosawa, T.; Lopez, J.; Katsumata, T., Intrinsically Stretchable and Healable Semiconducting Polymer for Organic Transistors. *Nature* **2016**, *539*, 411.
(9) Huang, W.; Jiao, H.; Huang, Q.; Zhang, J.; Zhang, M., Ultra-High Drivability, High-Mobility, Low-Voltage and High-Integration Intrinsically Stretchable Transistors. *Nanoscale* **2020**, DOI: 10.1039/D0NR05486K.
(10) Zhou, L.; Mao, J.; Ren, Y.; Han, S. T.; Roy, V. A.; Zhou, Y., Recent Advances of Flexible Data Storage Devices Based on Organic Nanoscaled Materials. *Small* **2018**, *14*, 1703126.
(11) Lai, Y.-C.; Huang, Y.-C.; Lin, T.-Y.; Wang, Y.-X.; Chang, C.-Y.; Li, Y.; Lin, T.-Y.; Ye, B.-W.; Hsieh, Y.-P.; Su, W.-F., Stretchable Organic Memory: Toward Learnable and Digitized Stretchable Electronic Applications. *NPG Asia Mater.* **2014**, *6*, e87-e87.
(12) Hsu, L.-C.; Shih, C.-C.; Hsieh, H.-C.; Chiang, Y.-C.; Wu, P.-H.; Chueh, C.-C.; Chen, W.-C., Intrinsically Stretchable, Solution-processable Functional Poly (siloxane-imide)s for Stretchable Resistive Memory Applications. *Polym. Chem.* **2018**, *9*, 5145-5154.
(13) Hammock, M. L.; Chortos, A.; Tee, B. C. K.; Tok, J. B. H.; Bao, Z., 25th Anniversary Article: the Evolution of Electronic Skin (E-skin): A Brief History, Design Considerations, and Recent Progress. *Adv. Mater.* **2013**, *25*, 5997-6038.
(14) Son, D.; Lee, J.; Qiao, S.; Ghaffari, R.; Kim, J.; Lee, J. E.; Song, C.; Kim, S. J.; Lee, D. J.; Jun, S. W., Multifunctional Wearable Devices for Diagnosis and Therapy of Movement Disorders. *Nat. Nanotechnol.* **2014**, *9*, 397.
(15) Jin, H.; Abu-Raya, Y. S.; Haick, H., Advanced Materials for Health Monitoring with Skin-based Wearable Devices. *Adv. Healthc. Mater.* **2017**, *6*, 1700024.
(16) Mishra, S.; Kim, Y.-S.; Intarasirisawat, J.; Kwon, Y.-T.; Lee, Y.; Mahmood, M.; Lim, H.-R.; Herbert, R.; Yu, K. J.; Ang, C. S., Soft, Wireless Periocular Wearable Electronics for Real-time Detection of Eye Vergence in a Virtual Reality Toward Mobile Eye Therapies. *Sci. Adv.* **2020**, *6*, eaay1729.
(17) Di, C. a.; Zhang, F.; Zhu, D., Multi-functional Integration of Organic Field-effect Transistors (OFETs): Advances and Perspectives. *Adv. Mater.* **2013**, *25*, 313-330.

(18) Ni, Y.; Wang, Y.; Xu, W., Recent Process of Flexible Transistor-Structured Memory. *Small* **2020**, 1905332.
(19) Leong, W. L.; Lee, P. S.; Lohani, A.; Lam, Y. M.; Chen, T.; Zhang, S.; Dodabalapur, A.; G. Mhaisalkar, S., Non-volatile Organic Memory Applications Enabled by In Situ Synthesis of Gold Nanoparticles in a Self-assembled Block Copolymer. *Adv. Mater.* **2008**, *20*, 2325-2331.
(20) Kang, M.; Baeg, K. J.; Khim, D.; Noh, Y. Y.; Kim, D. Y., Printed, Flexible, Organic Nano-floating-gate Memory: Effects of Metal Nanoparticles and Blocking Dielectrics on Memory Characteristics. *Adv. Funct. Mater.* **2013**, *23*, 3503-3512.
(21) Hoffman, J.; Pan, X.; Reiner, J. W.; Walker, F. J.; Han, J.; Ahn, C. H.; Ma, T., Ferroelectric Field Effect Transistors for Memory Applications. *Adv. Mater.* **2010**, *22*, 2957-2961.
(22) Naber, R. C.; Asadi, K.; Blom, P. W.; de Leeuw, D. M.; de Boer, B., Organic Nonvolatile Memory Devices Based on Ferroelectricity. *Adv. Mater.* **2010**, *22*, 933-945.
(23) Chiu, Y. C.; Otsuka, I.; Halila, S.; Borsali, R.; Chen, W. C., High-Performance Nonvolatile Transistor Memories of Pentacence Using the Green Electrets of Sugar-based Block Copolymers and Their Supramolecules. *Adv. Funct. Mater.* **2014**, *24*, 4240-4249.
(24) Chen, C.-H.; Wang, Y.; Michinobu, T.; Chang, S.-W.; Chiu, Y.-C.; Ke, C.-Y.; Liou, G.-S., Donor–Acceptor Effect of Carbazole-Based Conjugated Polymer Electrets on Photoresponsive Flash Organic Field-Effect Transistor Memories. *ACS Appl. Mater. Interfaces* **2020**, *12*, 6144-6150.
(25) Shih, C.-C.; Lee, W.-Y.; Chen, W.-C., Nanostructured Materials for Non-volatile Organic Transistor Memory Applications. *Mater. Horizons* **2016**, *3*, 294-308.
(26) Shih, C. C.; Chiu, Y. C.; Lee, W. Y.; Chen, J. Y.; Chen, W. C., Conjugated Polymer Nanoparticles as Nano Floating Gate Electrets for High Performance Nonvolatile Organic Transistor Memory Devices. *Adv. Funct. Mater.* **2015**, *25*, 1511-1519.
(27) Shih, C.-C.; Chiang, Y.-C.; Hsieh, H.-C.; Lin, Y.-C.; Chen, W.-C., Multilevel Photonic Transistor Memory Devices Using Conjugated/Insulated Polymer Blend Electrets. *ACS Appl. Mater. Interfaces* **2019**, *11*, 42429-42437.
(28) Ling, H.; Lin, J.; Yi, M.; Liu, B.; Li, W.; Lin, Z.; Xie, L.; Bao, Y.; Guo, F.; Huang, W., Synergistic Effects of Self-doped Nanostructures as Charge Trapping Elements in Organic Field Effect Transistor Memory. *ACS Appl. Mater. Interfaces* **2016**, *8*, 18969-18977.
(29) Hsu, J.-C.; Lee, W.-Y.; Wu, H.-C.; Sugiyama, K.; Hirao, A.; Chen, W.-C., Nonvolatile Memory Based on Pentacene Organic Field-effect Transistors with Polystyrene Para-substituted Oligofluorene Pendent Moieties as Polymer Electrets. *J. Mater. Chem.* **2012**, *22*, 5820-5827.
(30) Chiu, Y.-C.; Shih, C.-C.; Chen, W.-C., Nonvolatile Memories Using the Electrets of Conjugated Rod-Coil Block Copolymer and Its Nanocomposite with Single Wall Carbon Nanotubes. *J. Mater. Chem. C* **2015**, *3*, 551-558.
(31) Chiang, Y.-C.; Kobayashi, S.; Isono, T.; Shih, C.-C.; Shingu, T.; Hung, J.-J.; Hsieh, H.-C.; Tung, S.-H.; Satoh, T.; Chen, W.-C., Effect of Conjugated/Elastic Block Sequence On Morphology and Electronic Properties of Polythiophene Based Stretchable Block Copolymers. *Polym. Chem.* **2019**, *10*, 5452-5464.
(32) Hsu, L.-C.; Kobayashi, S.; Isono, T.; Chiang, Y.-C.; Ree, B. J.; Satoh, T.; Chen, W.-C., Highly Stretchable Semiconducting Polymers for Field-Effect Transistors through Branched Soft–Hard–Soft Type Triblock Copolymers. *Macromolecules* **2020**, *53*, 7496–7510.
(33) Hsieh, H.-C.; Hung, C.-C.; Watanabe, K.; Chen, J.-Y.; Chiu, Y.-C.; Isono, T.; Chiang, Y.-C.; Reghu, R. R.; Satoh, T.; Chen, W.-C., Unraveling the Stress Effects on the Optical Properties of Stretchable Rod-Coil Polyfluorene-Poly (n-butyl acrylate) Block Copolymer Thin Films. *Polym. Chem.* **2018**, *9*, 3820-3831.

(34) Isono, T.; Ree, B. J.; Tajima, K.; Borsali, R.; Satoh, T., Highly Ordered Cylinder Morphologies with 10 nm Scale Periodicity in Biomass-based Block Copolymers. *Macromolecules* **2018**, *51*, 428-437.
(35) Kobayashi, S.; Fujiwara, K.; Jiang, D.-H.; Yamamoto, T.; Tajima, K.; Yamamoto, Y.; Isono, T.; Satoh, T., Suzuki–Miyaura Catalyst-Transfer Polycondensation of Triolborate-Type Fluorene Monomer: Toward Rapid Access to Polyfluorene-Containing Block and Graft Copolymers from Various Macroinitiators. *Polym. Chem.* **2020.** DOI: 10.1039/D0PY01127D.
(36) Jiang, D.-H.; Kobayashi, S.; Jao, C.-C.; Mato, Y.; Isono, T.; Fang, Y.-H.; Lin, C.-C.; Satoh, T.; Tung, S.-H.; Kuo, C.-C., Light Down-Converter Based on Luminescent Nanofibers from the Blending of Conjugated Rod-Coil Block Copolymers and Perovskite through Electrospinning. *Polymers* **2020**, *12*, 84.
(37) Chen, S.; Su, A.; Su, C.; Chen, S., Phase Behavior of Poly (9, 9-di-n-hexyl-2, 7-fluorene). *J. Phys. Chem. B* **2006**, *110*, 4007-4013.
(38) Xu, J.-T.; Fairclough, J. P. A.; Mai, S.-M.; Chaibundit, C.; Mingvanish, M.; Booth, C.; Ryan, A. J., Crystallization Behavior of Oxyethylene/Oxybutylene Diblock and Triblock Copolymers. *Polymer* **2003**, *44*, 6843-6850.
(39) Tzavalas, S.; Mouzakis, D. E.; Drakonakis, V.; Gregoriou, V. G., Polyethylene Terephthalate–Multiwall Nanotubes Nanocomposites: Effect of Nanotubes on the Conformations, Crystallinity and Crystallization Behavior of PET. *J. Polym. Sci., Part B: Polym. Phys.* **2008**, *46*, 668-676.
(40) Liu, C.; Chan, K. W.; Shen, J.; Liao, C. Z.; Yeung, K. W. K.; Tjong, S. C., Polyetheretherketone Hybrid Composites with Bioactive Nanohydroxyapatite and Multiwalled Carbon Nanotube Fillers. *Polymers* **2016**, *8*, 425.
(41) Wu, W.-R.; Chuang, W.-T.; Jeng, U.-S.; Su, C.-J.; Chen, S.-H.; Chen, C.-Y.; Su, C.-H.; Su, A.-C., Effects of Mesomorphic β Nanograins on Crystallization and Photoexcited Emission of Poly (9, 9-di-n-hexyl-2, 7-fluorene). *Polymer* **2012**, *53*, 3928-3936.
(42) Persson, N. E.; McBride, M. A.; Grover, M. A.; Reichmanis, E., Automated analysis of orientational order in images of fibrillar materials. *Chem. Mater.* **2017**, *29*, 3-14.
(43) Liu, J.; Wang, Q.; Liu, C.; Chang, H.; Tian, H.; Geng, Y.; Yan, D., Melt-crystallized α phase nanofibril films of monodisperse poly (9, 9-dioctylfluorene). *Polymer* **2015**, *65*, 1-8.
(44) Kim, C.-H.; Kymissis, I., Graphene–organic hybrid electronics. *J. Mater. Chem. C* **2017**, *5*, 4598-4613.

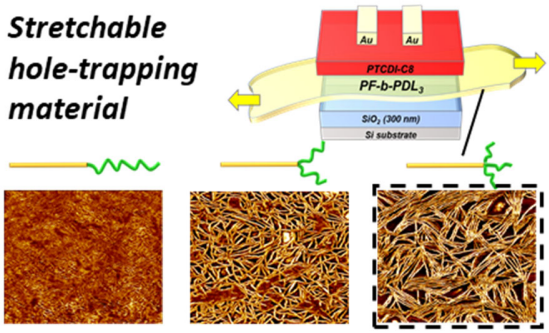

For Table of Contents Only